Meccanica (2016) 51:429–441
DOI 10.1007/s11012-015-0281-2



# Neighborhood influences on stress and strain partitioning in dual-phase microstructures

## An investigation on synthetic polycrystals with a robust spectral-based numerical method

**Martin Diehl · Pratheek Shanthraj · Philip Eisenlohr · Franz Roters**

Received: 28 August 2015 / Accepted: 4 September 2015 / Published online: 28 October 2015


**Abstract** The mechanical response of multiphase metallic materials is governed by the strain and stress partitioning behavior among their phases, crystals, and subgrains. Despite knowledge about the existence of these complex and long-ranging interactions, the experimental characterization of such materials is often limited to surface observations of microstructure evolution and strain partitioning, i.e. ignoring the influence of the underlying features. Hence, for the interpretation of the observed surface behavior it is imperative to understand how it might be influenced by the subsurface microstructure. In the present study, we therefore systematically change the subsurface microstructure of synthetic dual-phase polycrystals and investigate the altered response of a 2D region of interest. The series of high-resolution crystal plasticity simulations are conducted with a fast and efficient spectral-based iterative scheme for calculating the mechanical response of complex crystalline materials. To overcome the slow convergence of the conventional spectral-based solver when dealing with heterogeneous materials of large contrast in stiffness (or strength), direct and mixed variational conditions for mechanical equilibrium and strain compatibility have been formulated such that they can be combined with a general class of non-linear solution methods. The different solution techniques have been implemented into DAMASK, the Düsseldorf Advanced Material Simulation Kit, and the ones showing the best performance are used in this study. The results show that the subsurface microstructure has a dominant influence on the observed stress and strain partitioning. Additionally, it can be seen that the zone of influence increases with increasing heterogeneity of the microstructure.

**Keywords** Crystal plasticity · Dual-phase steel · Spectral method · Voronoi tessellation · Stress and strain partitioning

M. Diehl (✉) · P. Shanthraj · F. Roters
Microstructure Physics and Alloy Design, Max-Planck-Institut für Eisenforschung GmbH, Max-Planck-Str. 1, 40237 Düsseldorf, Germany
e-mail: m.diehl@mpie.de

P. Shanthraj
e-mail: p.shanthraj@mpie.de

F. Roters
e-mail: f.roters@mpie.de

P. Shanthraj
Aachen Institute for Advanced Study in Computational Engineering Science, RWTH Aachen University, Schinkelstraße 2, 52062 Aachen, Germany

P. Eisenlohr
Chemical Engineering and Materials Science, Michigan State University, 428 S. Shaw Lane, East Lansing, MI 48824-1226, USA
e-mail: eisenlohr@egr.msu.edu

## 1 Introduction

Dual-phase (DP) steels are a prominent example of metallic composite materials that gain their excellent

mechanical properties from a complex interplay among their phases, crystals, and subgrains [24]. DP steels consists of mainly two phases, a softer ferritic matrix with hard martensitic inclusions for simultaneous improvement of strength and ductility. Despite their wide use in automotive applications and a large number of works investigating the mechanical behavior of DP steels, a full understanding of the local stress and strain partitioning—that is responsible for their excellent mechanical properties—is not yet achieved.

Current crystal plasticity (CP) based simulation techniques, on the one hand, enable investigation of strain and stress partitioning effects at the scale of grains and subgrains taking the full 3D microstructure into account [2]. On the other hand, even recent simulation approaches that aim at comparing experimental and simulated results [18, 22] are limited to two dimensions due to experimental limitations. More precisely, the acquisition of 3D strain maps via digital volume correlation or of stress partitioning via X-ray diffraction is associated with high efforts. Hence, even though Landron et al. [7] presented a study on void coalescence in 3D, most of the investigations on DP micromechanics are still limited to surface measurements of microstructural features and—with the help of digital image correlation—strain partitioning.

In this study, we therefore investigate the effect of subsurface features—that are difficult to obtain non-destructively—on responses measured at the surface. The pioneering work of Zeghadi et al. [28, 29] has already outlined the importance of subsurface microstructure. Here, we extend their investigations to the case of a dual-phase microstructure. Moreover, we try to quantify the size of the region of influence by systematically evaluating the interactions of microstructural features in relation to the distance to the region of interest (ROI, usually being the surface). In contrast to Ramazani et al. [17], who investigated the correlation of predicted macroscopic stress–strain relations between 2D and 3D simulations, the present study focuses on *local* stress and strain partitioning in DP steels.

The remainder of the paper is organized as follows. In Sect. 2 the numerical solution method is outlined and the constitutive description, geometrical setup, and boundary conditions used in the simulations are presented. Corresponding results are given and discussed in Sect. 3 with Sect. 4 providing a summary along with perspectives for future applications.

## 2 Simulation setup

### 2.1 Numerical solution strategy

Micromechanical simulation of dual-phase (ferrite and martensite) grain aggregates demands a methodology that is numerically efficient, i.e., fast and capable of high spatial resolution, and can cope with large variations in material properties, i.e., large property contrast. Moulinec and Suquet [15] presented a spectral method approach for the solution of periodic mechanical boundary value problems in the context of elastic composites. Since stress equilibrium is calculated in FOURIER space, the use of fast FOURIER transforms (FFT) allows for a very time- and memory-efficient iterative solution algorithm. Moreover, since its ansatz functions are trigonometric polynomials defined over the whole domain, its solution quality commonly exceeds the finite element method (FEM) using piecewise-defined low-order polynomials.

The application of this methodology to the case of viscoplastic polycrystals was pioneered by Lebensohn [8] and applied in numerous studies, e.g., [9, 11, 12, 21]. For more heterogenous materials, however, the slow convergence of the original fixpoint iterative method when facing a large contrast in the local stiffness is prohibitive [13]. Several approaches have been proposed to overcome this limitation. Eyre and Milton [4] and Monchiet and Bonnet [14] introduced accelerated schemes for materials with large property contrasts. For the case of infinite property contrasts, Michel et al. [13] suggested a method based on augmented LAGRANGIANS. Improved convergence compared to the original approach has also been demonstrated through the use of advanced solution methods [1, 30] in lieu of fixpoint iteration.

Eisenlohr et al. [3] generalized the spectral methodology to use arbitrary constitutive material descriptions within a finite-strain framework following the work of Lahellec et al. [6]. In addition, we recently introduced direct and mixed variational formulations within the same finite-strain CP framework and benchmarked them using various non-linear solution methods [20]. In the present study, the Düsseldorf Advanced Material Simulation Kit (DAMASK, http://damask.mpie.de/) and its associated spectral solver are employed with the direct variational formulation (analogous to the "basic scheme" [6]) being selected for all simulations except

for the 2D simulations, for which one version of the mixed variational formulation (analogous to the "polarization scheme" [14]) is selected—both in combination with GMRES [16] as solution algorithm (see [20] for details).

### 2.2 Constitutive model

At each material point, the deformation gradient $\boldsymbol{F}(\boldsymbol{x})$ is multiplicatively decomposed into elastic and plastic components as $\boldsymbol{F} = \boldsymbol{F}_\mathrm{e}\boldsymbol{F}_\mathrm{p}$. An anisotropic elastic stiffness $\mathbb{C}$ relates the elastic deformation gradient $\boldsymbol{F}_\mathrm{e}$ to the second PIOLA–KIRCHHOFF stress by $\boldsymbol{S} = \mathbb{C}\,(\boldsymbol{F}_\mathrm{e}{}^\mathrm{T}\boldsymbol{F}_\mathrm{e} - \boldsymbol{I})/2$. The plastic velocity gradient $\boldsymbol{L}_\mathrm{p} = \dot{\boldsymbol{F}}_\mathrm{p}\boldsymbol{F}_{\mathrm{p}^{-1}}$ is implicitly driven by $\boldsymbol{S}$ by virtue of the chosen plasticity model, which in the present study is an adoption of the phenomenological description of Hutchinson [5] for body-centered cubic crystals (for details see [19]). The microstructure is parameterized in terms of a slip resistance $g^\alpha$ on each of the twelve $\langle 111\rangle\{110\}$ and $\langle 111\rangle\{112\}$ slip systems, which are indexed by $\alpha = 1,\ldots,24$. These resistances evolve asymptotically from $g_0$ towards $g_\infty$ with shear $\gamma^\beta$ ($\beta = 1,\ldots,24$) according to the relationship

$$\dot{g}^\alpha = \dot{g}^\beta\, h_0 \left|1 - g^\beta/g^\beta_\infty\right|^a \mathrm{sgn}\left(1 - g^\beta/g^\beta_\infty\right) h_{\alpha\beta} \qquad (1)$$

with parameters $h_0$ and $a$. The interaction between different slip systems is captured by the hardening matrix $h_{\alpha\beta}$. Given a set of current slip resistances, shear on each system occurs at a rate

$$\dot{\gamma}^\alpha = \dot{\gamma}_0 \left|\frac{\tau^\alpha}{g^\alpha}\right|^n \mathrm{sgn}(\tau^\alpha) \qquad (2)$$

with $\dot{\gamma}_0$ as reference shear rate, $\tau^\alpha = \boldsymbol{S}\cdot(\boldsymbol{s}^\alpha \otimes \boldsymbol{n}^\alpha)$, and $n$ the stress exponent. The superposition of shear on all slip systems in turn determines the plastic velocity gradient

$$\boldsymbol{L}_\mathrm{p} = \dot{\gamma}^\alpha \boldsymbol{s}^\alpha \otimes \boldsymbol{n}^\alpha, \qquad (3)$$

where $\boldsymbol{s}^\alpha$ and $\boldsymbol{n}^\alpha$ are unit vectors along the slip direction and slip plane normal, respectively.

### 2.3 Constitutive parameters

The parameters specifying the mechanical behavior of ferrite and martensite are the same ones used by Tasan et al. [23] for a joint experimental–numerical analysis of stress and strain partitioning in DP steels (see Table 1). Since the use of realistic phase parameters is a crucial point in CP modelling, we briefly recapitulate the phase properties determination procedure in the following:

An inverse optimization strategy based on matching simulated and measured indentation topographies [26, 27] is applied to the case of body-centered cubic crystal structure of ferrite to determine its parameters for the CP model. The procedure iteratively fits initial and final shear resistance of the $\langle 111\rangle\{110\}$ and $\langle 111\rangle\{112\}$ slip system families such that the pile-up topography resulting from load-controlled nanoindentation using a sphero-conical diamond tip in four large and differently oriented grains is correctly predicted by CPFEM simulations. The optimization relies on a NELDER–MEAD algorithm with the objective function considering differences in pile-up topographies and load–displacement curves between CPFEM simulation and experimental data. Employing the DAMASK framework allows to use exactly the same constitutive model for both, the parameter identification with the commercial FEM solver MSC.MARC as well as for subsequent simulation of the DP microstructures with the fast and efficient spectral solver.

**Table 1** Material parameters, based on [25] and adjusted to actual phase properties. Initial and saturation slip resistance values for ferrite are determined by an inverse simulation procedure and for martensite by fitting to stress–strain curve and hardness ratio

| Property | Value | | Unit |
|---|---|---|---|
| | Ferrite | Martensite | |
| $C_{11}$ | 233.3 | 417.4 | GPa |
| $C_{12}$ | 135.5 | 242.4 | GPa |
| $C_{44}$ | 118.0 | 211.1 | GPa |
| $g_{0,\{110\}}$ | 95 | 406 | MPa |
| $g_{\infty,\{110\}}$ | 222 | 873 | MPa |
| $g_{0,\{112\}}$ | 97 | 457 | MPa |
| $g_{\infty,\{112\}}$ | 412 | 971 | MPa |
| $h_0$ | 1 | 563 | GPa |
| $h_{\alpha\beta}$ | 1 | 1 | |
| $\dot{\gamma}_0$ | 1 | 1 | $10^{-3}/\mathrm{s}$ |
| $n$ | 20 | 20 | |
| $a$ | 2.0 | 2.0 | |

The indentation procedure is not applicable to the martensitic phase due to resolution limitations of the experimental setup. Therefore, constitutive parameter values fitted to the macroscopic, i.e. polycrystal, stress–strain curve of a purely martensitic steel are selected. Out of these parameters, the initial and final shear resistance are further adjusted to match the ratio between ferrite and martensite flow stress identified from nanoindentation experiments in both phases of the material at hand.

## 2.4 Microstructures

Three periodic, artificial grain structures, each filling a unit cube, are created by a standard Voronoi tessellation approach based on 400 randomly[1] placed seed points each. These structures, referred to as "A", "B", and "C", are discretized by a regular voxel grid with each of the $100 \times 100 \times 100$ grid points being associated to its nearest (periodically repeated) seed point such that a space partitioning of 400 "grains" results. All grid points of one grain are designated the same phase (ferritic or martensitic) with initially homogeneous and randomly chosen lattice orientation. For each of the three microstructures, a *number* fraction $n_{\text{mart}} = 0.1$, 0.2, and 0.4 of the grains are randomly selected as martensitic, resulting in martensite *volume* fractions of 0.0924–0.1123, 0.1841–0.2056, and 0.3883–0.4062, respectively. The resulting nine initial microstructures colored according to the inverse pole figure (IPF) along the normal direction are given in Fig. 1.

### 2.4.1 Grain orientation variation

To investigate how the kinematic response at a surface is influenced by the subsurface grain structure, 27 variants of the initial 9 microstructures are created by randomly altering the *lattice orientation* of grains that belong to Voronoi seed points within a slice of thickness $t = 0.2$ centered at the plane $\Delta z = 0.3$, 0.5, or 0.7 below the surface (being at $z = 1$). No values $\Delta z < 0.3$ are considered, since the Voronoi seed of grains observable at $z = 1$ (i.e. the ROI at the surface) might be located in the affected volume and, hence, their lattice orientation would be changed.

[1] Ensuring that at least one voxel is assigned to each seed point when discretizing on a $64^3$ voxel grid.

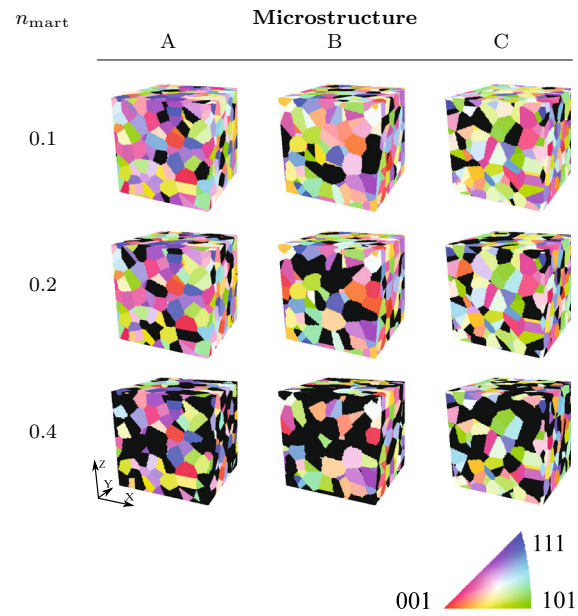


**Fig. 1** Periodic microstructures A, B, and C (*left* to *right*) discretized by $100^3$ points and containing a total of 400 grains. *Black color* indicates martensite grains with number fraction of $n_{\text{mart}} = 0.1$, 0.2, and 0.4 (*top* to *bottom*). Color map at lower right encodes crystal orientation parallel to $z$ (IPF) used in this study

A "buffer zone" of height 0.2 (corresponding to 20 additional voxel layers along $z$) and elastic-isotropic behavior with $C_{11} = 20.0\,\text{GPa}$ and $C_{12} = 13.3\,\text{GPa}$ is added in between periodic repetitions of the microstructure (see Fig. 2 top). Introduction of this buffer zone results in boundary conditions that are reminiscent of free surfaces above and below the polycrystalline structure, similar to a thick free-standing film.

### 2.4.2 Grain shape variation

In the same spirit as for the grain orientation variation, 27 variants of the initial 9 microstructures are created by randomly altering the *position* of Voronoi seed points within a slice of thickness $t = 0.2$ centered at the plane $\Delta z = 0.3$, 0.5, or 0.7 below the surface ($z = 1$). A change in seed point position is limited to a distance of the equivalent average grain diameter.[2] As a consequence of altered seed positions, the

[2] $400\,(d_{\text{eq}}/2)^3\,4\,\pi/3 = 1^3$

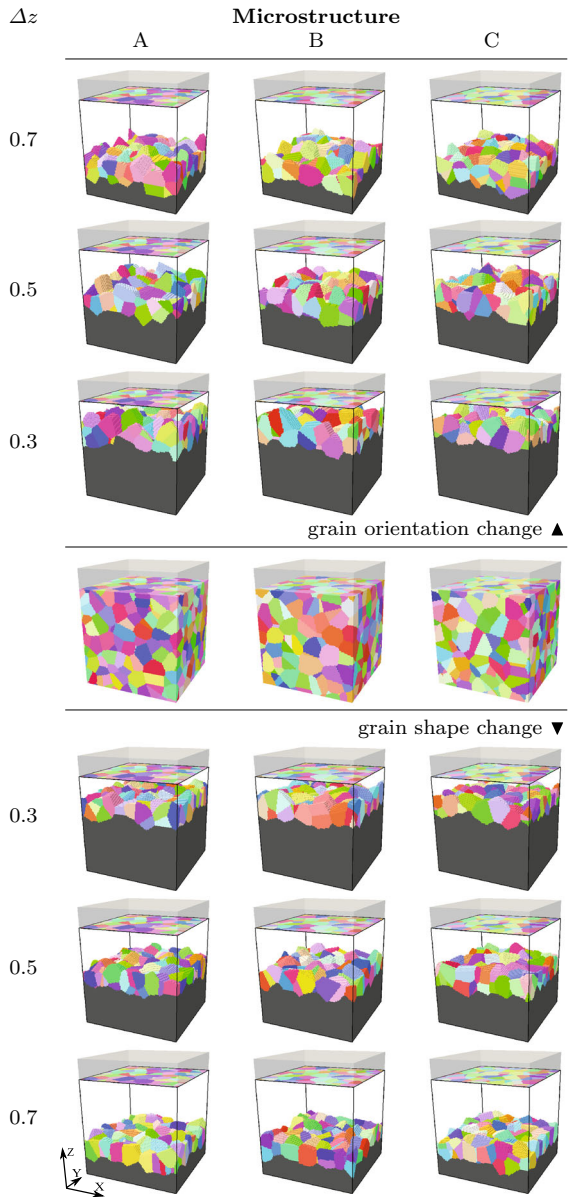


**Fig. 2** Localized variation of grain *orientation* (*top*) and *shape* (*bottom*). Grains whose VORONOI seed points fall within a layer of thickness $t = 0.2$ centered $\Delta z$ below the surface have altered lattice orientation (*top*) or shape and position (*bottom*) relative to the unaltered structure (indicated as transparent above and *dark gray* below altered layer). *Translucent gray* volume corresponds to a "buffer zone" of negligible stiffness mimicking a free surface. For IPF legend see Fig. 1

tessellation results in differently shaped grains in the vicinity of the affected plane (see Fig. 2 bottom). Values $\Delta z < 0.3$ are excluded as the geometry of the grain structure observable at the ROI might be changed by altering the seed point coordinates close to this (surface) plane. Again, to mimic the effect of a free surface at the ROI, a "buffer zone" consisting of the same soft material is added in between periodic repetitions of the microstructure (see Fig. 2), resulting in "thick film" behavior.

### 2.4.3 *Grain columnarity variation*

To establish the distance up to which the deformation behavior of a ROI is influenced by grain interactions within a *bulk* polycrystal, the height of the periodic grain structure introduced in Sect. 2.4 is progressively reduced to $h = 0.9, 0.8, \ldots, 0.3$[3] in a symmetric fashion around the plane $z = 0.5$. The VORONOI tessellation of the periodically repeated volume includes only seed points with $-h/2 < z - 0.5 \leq +h/2$. As the number of unique grains decreases with height reduction, the neighborhood around the central $x$–$y$ plane is gradually altered and turns progressively more columnar.[4] Additionally, the limiting case of repeating only the ROI layer ($h = 0.01$, i.e. assuming fully columnar grains as a consequence of the periodic boundary conditions) is investigated. Figure 3 presents exemplary microstructures of various heights for all three structures with martensite grain fraction $n_{\text{mart}} = 0.2$ (corresponding to the center row in Fig. 1). Here, no buffer zone is interspersed, since bulk polycrystal properties are targeted.

## 2.5 Loading

The volume elements (VEs) were subjected to loading in $x$-direction, i.e. the ROI is deformed in-plane, commensurate with the surface of a tensile deformation sample. For the grain orientation variation and grain shape variation a constant true strain rate of $L_{xx} = 10^{-3}\,\text{s}^{-1}$ and $L_{\text{yy}} = -10^{-3}\,\text{s}^{-1}$ was applied. Since the soft layer mimics a free surface, no stress boundary conditions are given and the remaining components of $\boldsymbol{F}$ remain constant. After a loading time of 46 s, the final deformation gradient prescribing plane strain is

[3] $h < 0.3$ resulted in changes of the grain structure slice at $z = 0.5$ and was therefore not considered.

[4] Columnarity is defined as the fraction of points along $z$ that share the same orientation as the points on the central $x$–$y$ plane.

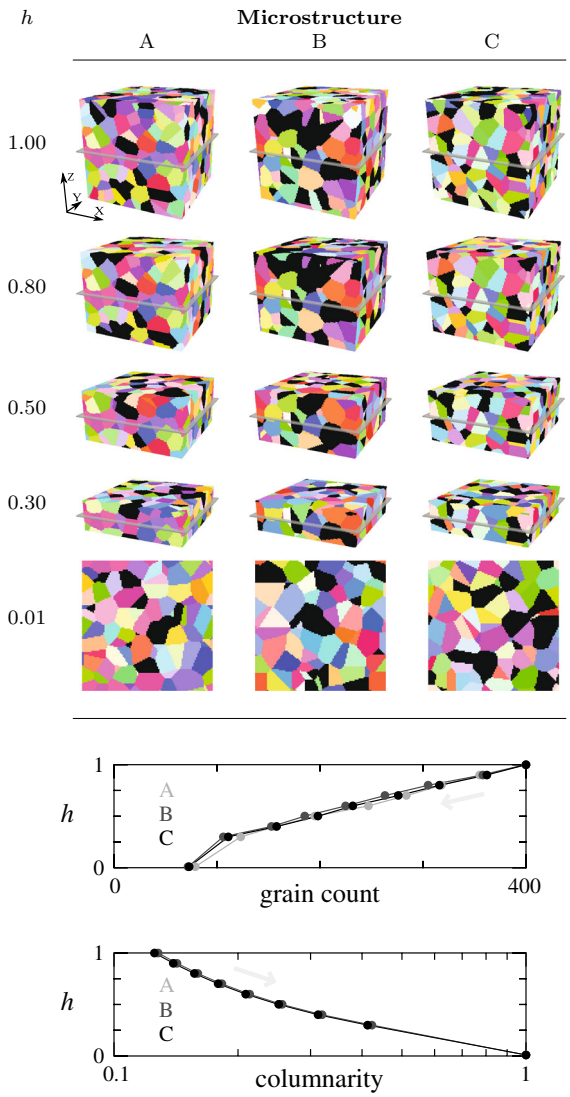


**Fig. 3** Variation of grain columnarity at the central $x$–$y$ plane (ROI, indicated by the *light gray* slice and corresponding to the structure for $h = 0.01$) through symmetrical reduction of height $h$ of the initial microstructures. Since volume elements are fully periodic, the number of unique grains in each structure decreases and consequently the columnarity increases with reduction of the repetition period $h$ along $z$. Variants with $n_{\text{mart}} = 0.2$, indicated by *black color*, are shown as examples. For IPF legend see Fig. 1

$$\boldsymbol{F} = \begin{bmatrix} 1.047 & 0 & 0 \\ 0 & 0.955 & 0 \\ 0 & 0 & 1 \end{bmatrix}.$$

For the grain columnarity variation, a constant engineering strain rate of $\dot{F}_{xx} = 10^{-3}\text{s}^{-1}$ was applied. The deformation gradient in $y$- and $z$-direction was adjusted such that the average PIOLA–KIRCHHOFF stress in these directions vanished. This plane-stress boundary condition was applied for 82 s, resulting in a final deformation gradient

$$\boldsymbol{F} = \begin{bmatrix} 1.082* & * & \\ 0* & * & \\ 0 & 0 & * \end{bmatrix},$$

where asterisks "*" indicate components for which the corresponding components of $\boldsymbol{P}$ are enforced to be zero.

### 2.6 Mesh convergence and comparison to finite element methodology

We investigate the grid sensitivity by comparing microstructure B (with $n_{\text{mart}} = 0.2$) variants with $32^3$ and $64^3$ voxel resolution while keeping loading and material parameters as outlined above. The results presented in Fig. 4 (top) show no substantial difference in strain partitioning above $32^3$ from which we conclude that the resolution chosen in this study is sufficiently high to exclude mesh dependency.

Secondly, to confirm that the introduction of a softer "buffer layer" is equivalent to boundary conditions of a free surface, a comparison to simulation results using the FEM[5] with linear shape functions is performed. For the FEM simulations, a free surface with a normal along the $z$-direction and periodic boundary conditions in $x$- and $y$-direction are employed. As already observed by Eisenlohr et al. [3], the strain partitioning in the FEM solutions (Fig. 4 bottom) lacks fidelity but nevertheless they closely match the corresponding results of the spectral method simulations in a qualitative and quantitative way. In agreement with, for instance, Lebensohn et al. [10], we conclude that the chosen approach is valid for the present investigation.

## 3 Results and discussion

In the following, the partitioning of equivalent VON MISES strain ($\varepsilon_{\text{vM}}$) and stress ($\sigma_{\text{vM}}$) resulting from variation of grain shape, orientation, and columnarity

[5] MSC.MARC version 2014.1.

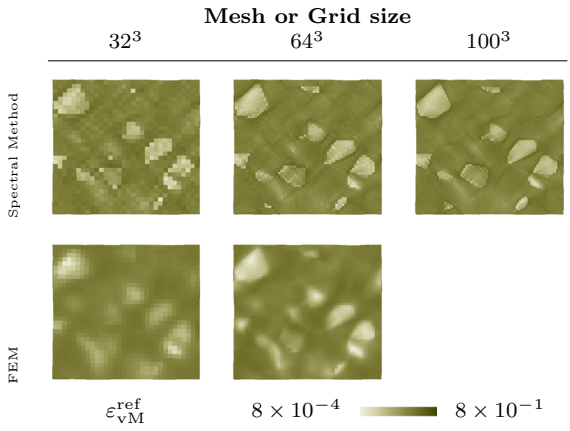


**Fig. 4** $\varepsilon_{\mathrm{vM}}^{\mathrm{ref}}$ of microstructure B at $z = 1$ (surface) for $n_{\mathrm{mart}} = 0.2$ calculated with different resolutions and solvers

are given. For the analysis, the absolute difference $\Delta p$ is defined as $\Delta p := p - p^{\mathrm{ref}}$ for $p \in \sigma_{\mathrm{vM}}, \varepsilon_{\mathrm{vM}}$ where the reference value $p^{\mathrm{ref}}$ is the one obtained from the unaltered microstructure. A (logarithmic) relative change is introduced as $\ln\left(1 + \Delta p / p^{\mathrm{ref}}\right)$, which is advantageous due to its symmetric behavior for large relative differences $\Delta p / p^{\mathrm{ref}}$.

For all three simulation studies, ROI maps of reference values and relative changes in equivalent VON MISES strain and stress are presented. Additionally, surface data is counted among all three microstructures (totalling $3 \times 100 \times 100$ voxels) and plotted for each phase (ferrite and martensite) in two different "heat map" (probability density) styles. The first heat map pair correlates absolute differences between equivalent stress and strain. The second pair plots the relative changes in strain as function of the distance $d_{\mathrm{PhaseBoundary}}$ to the nearest phase boundary (in voxels measured in the undeformed configuration). In both types of charts, the logarithmic gray scale ranges from none to all of the material points of each phase falling into the respective property combination bin.

### 3.1 Grain orientation variation

The partitioning of stress and strain within ferrite and martensite can easily be recognized in Fig. 5 due to the markedly different behavior of both phases. This partitioning is noticeably altered when the subsurface microstructure is modified at a distance of $\Delta z = 0.3$

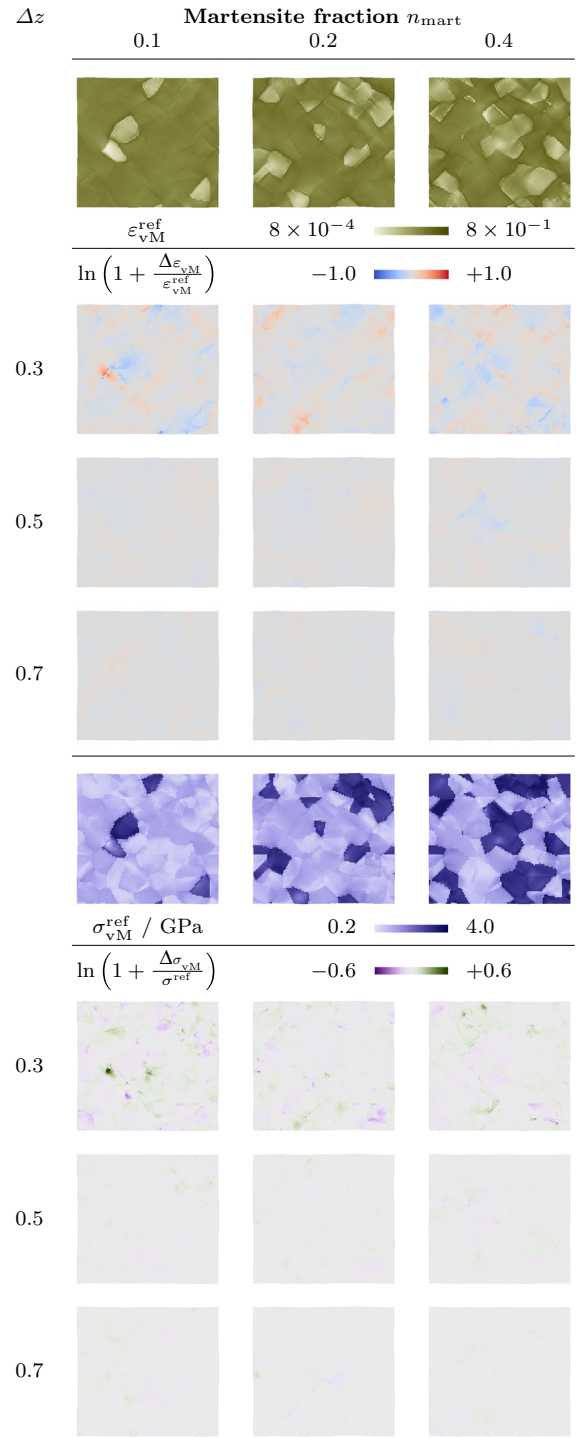


**Fig. 5** $\varepsilon_{\mathrm{vM}}^{\mathrm{ref}}$ (*top*) and $\sigma_{\mathrm{vM}}^{\mathrm{ref}}$ (*bottom*) of microstructure A at $z = 1$ and the sequence of relative strain and stress changes resulting from grain orientation variation at $\Delta z = 0.3,\ 0.5,\ 0.7$ with $n_{\mathrm{mart}} = 0.1, 0.2, 0.4$

below the surface, but no significant influence can be seen for modifications of the VE that occur further ($\Delta z = 0.5$, and 0.7) below the observed surface.

The combined surface data of all three variants, given in Fig. 6, confirms above observations: Substantial alterations of stress or strain are found when grain orientations change within a narrow subsurface region, i.e., at $\Delta z = 0.3$. For distances $\Delta z \geq 0.5$, almost no influence on the ROI can be observed. Hence, with an average grain size diameter $d_{\mathrm{eq}} \approx 0.17$, the zone of influence is confined to up to three subsurface grains, which is slightly larger than the lower-bound value of two grains reported by Zeghadi et al. [28] for the case of single phase polycrystals, and seems not to depend on the volume fraction of hard phase. Additionally, the dependence of relative changes in strain on the distance to a phase boundary (Fig. 7) reveals that volumes close to a boundary are generally more strongly affected by the grain orientation variation than locations in the phase center since the observed

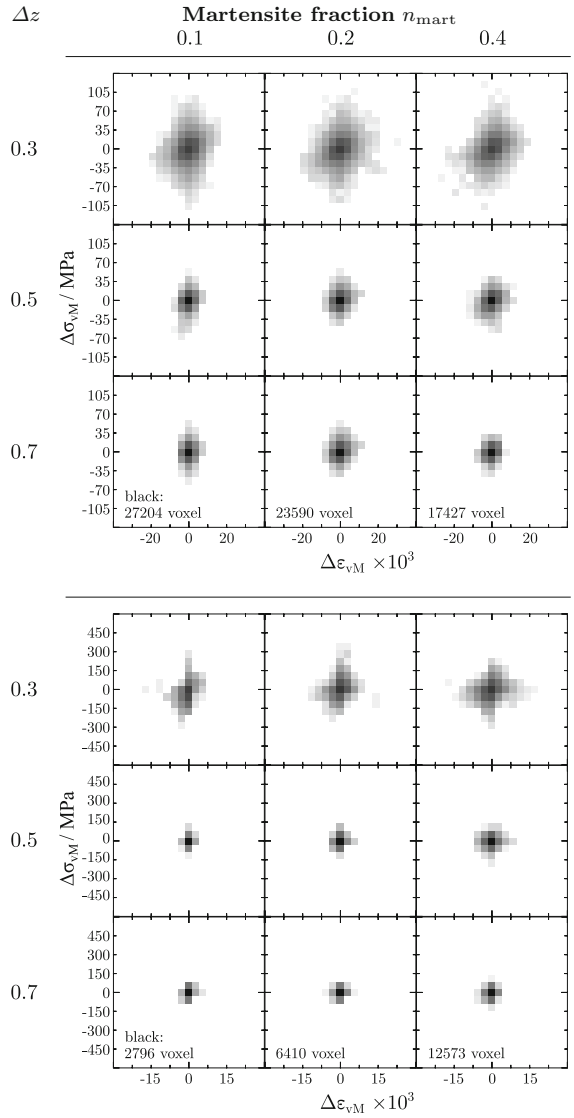


**Fig. 6** Correlation between $\Delta\sigma_{\mathrm{vM}}$ and $\Delta\varepsilon_{\mathrm{vM}}$ in ferrite (*top*) and martensite (*bottom*) resulting from grain orientation variation at $\Delta z = 0.3$, 0.5, 0.7 with $n_{\mathrm{mart}} = 0.1$, 0.2, 0.4

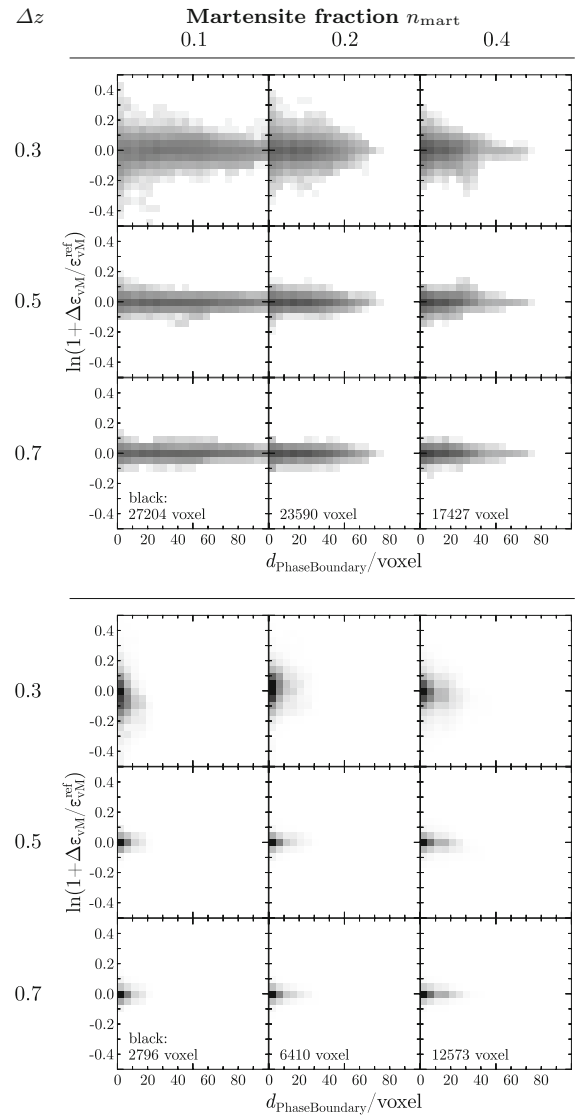


**Fig. 7** Correlation between relative strain change and distance to a phase boundary for ferrite (*top*) and martensite (*bottom*) resulting from grain orientation variation at $\Delta z = 0.3$, 0.5, 0.7 with $n_{\mathrm{mart}} = 0.1$, 0.2, 0.4

spread increases with decreasing $d_{\text{PhaseBoundary}}$. This spreading is not a strong function of $n_{\text{mart}}$, except for the geometric effect that the probability for larger $d_{\text{PhaseBoundary}}$ increases (decreases) for martensite (ferrite) with increasing $n_{\text{mart}}$. In comparison to the spread observed for the softer ferritic phase, the spread in the harder martensitic phase is notably narrower (compare Fig. 7 top to bottom).

### 3.2 Grain shape variation

Stress and strain for microstructure C at the free surface ($z = 1.0$) are mapped in Fig. 8. The influence of a microstructural modification at a distance of $\Delta z = 0.3$ to the surface is—as expected—the strongest among the cases investigated. Similar to the grain orientation variation, relative changes in strain are larger than those in stress. In contrast to the response observed for grain orientation variation, these changes are not largely independent of martensite content but grow with increasing $n_{\text{mart}}$ (compare Fig. 6 with 9). Overall, the magnitude of changes is larger than those observed for grain orientation variation (compare Fig. 5 with 8 or Fig. 7 with 10).

By comparing results between the grain orientation variation and the grain shape variation, three observations can be made:

1. The effect of the grain shape variation is stronger than that of the grain orientation variation at the same distance $\Delta z$ to the ROI.
2. The zone affected by a grain shape variation is larger than that affected by a grain orientation variation.
3. The depth of the affected zone when varying the grain shape notably depends on the martensite volume fraction—in contrast to only a minor influence when varying the grain orientation (Fig. 7, bottom). A higher martensite volume fraction correlates with a more pronounced effect on the stress and strain partitioning for a given distance.

### 3.3 Grain columnarity variation

Since the results of the grain columnarity variation are obtained with a different load case and especially at a higher strain level, a much wider range of stress and strain deviation from the reference case ($h = 1$) is

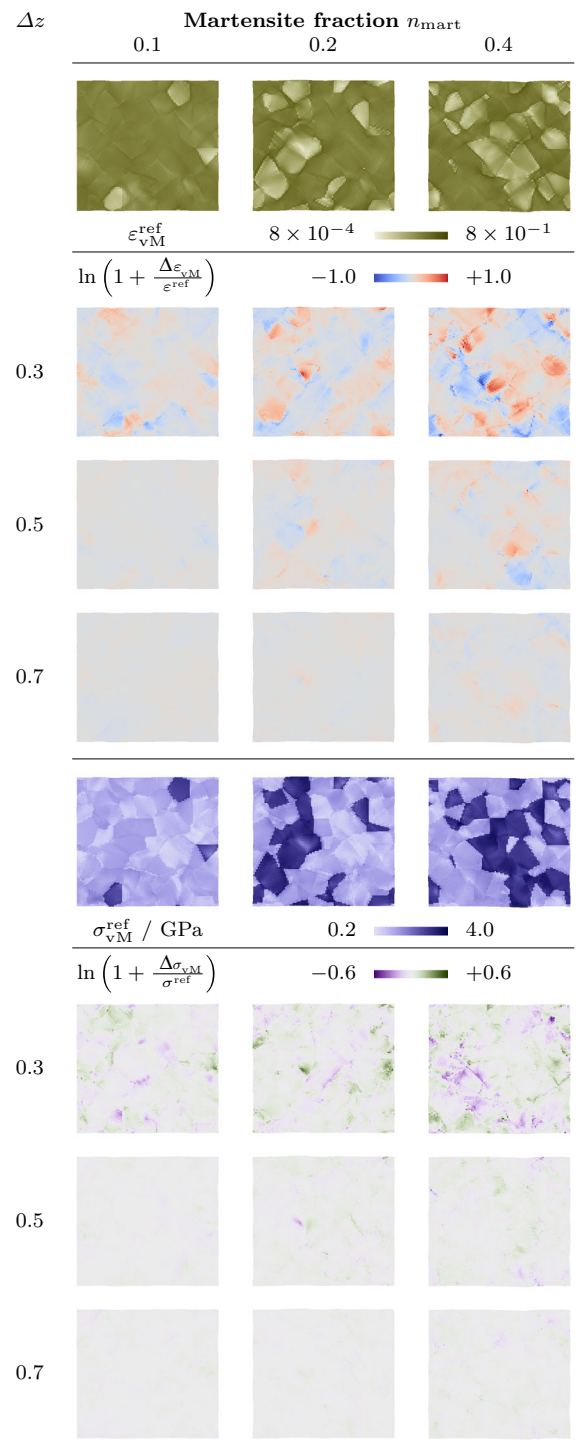


**Fig. 8** $\varepsilon_{\text{vM}}^{\text{ref}}$ (*top*) and $\sigma_{\text{vM}}^{\text{ref}}$ (*bottom*) of microstructure C at $z = 1$ and the sequence of relative strain and stress changes resulting from grain shape variation at $\Delta z = 0.3, 0.5, 0.7$ with $n_{\text{mart}} = 0.1$, 0.2, 0.4

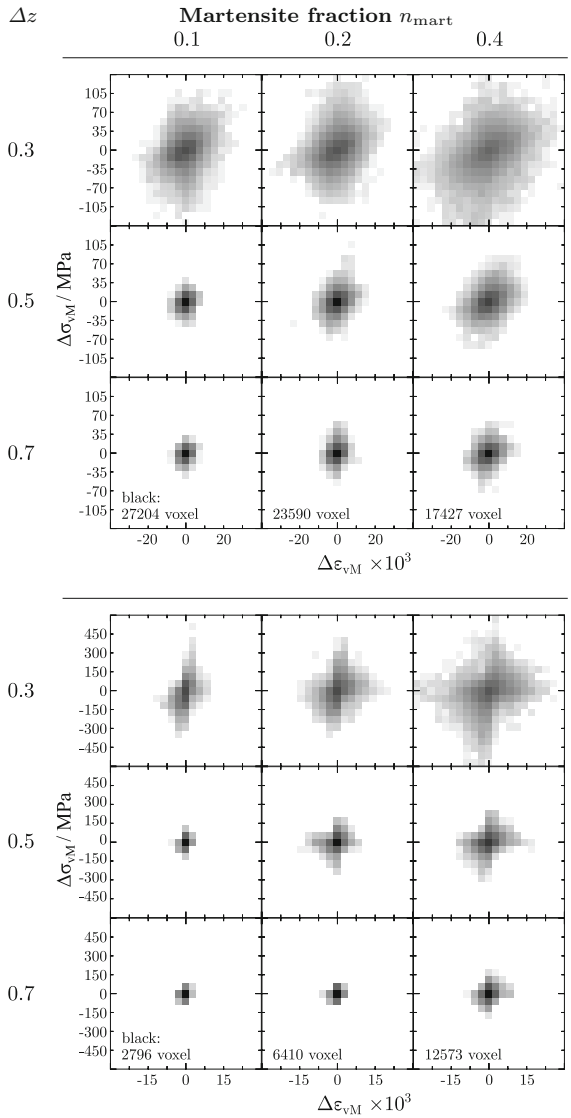


**Fig. 9** Correlation between $\Delta\sigma_{vM}$ and $\Delta\varepsilon_{vM}$ in ferrite (*top*) and martensite (*bottom*) resulting from grain shape variation at $\Delta z = 0.3, 0.5, 0.7$ with $n_{mart} = 0.1, 0.2, 0.4$

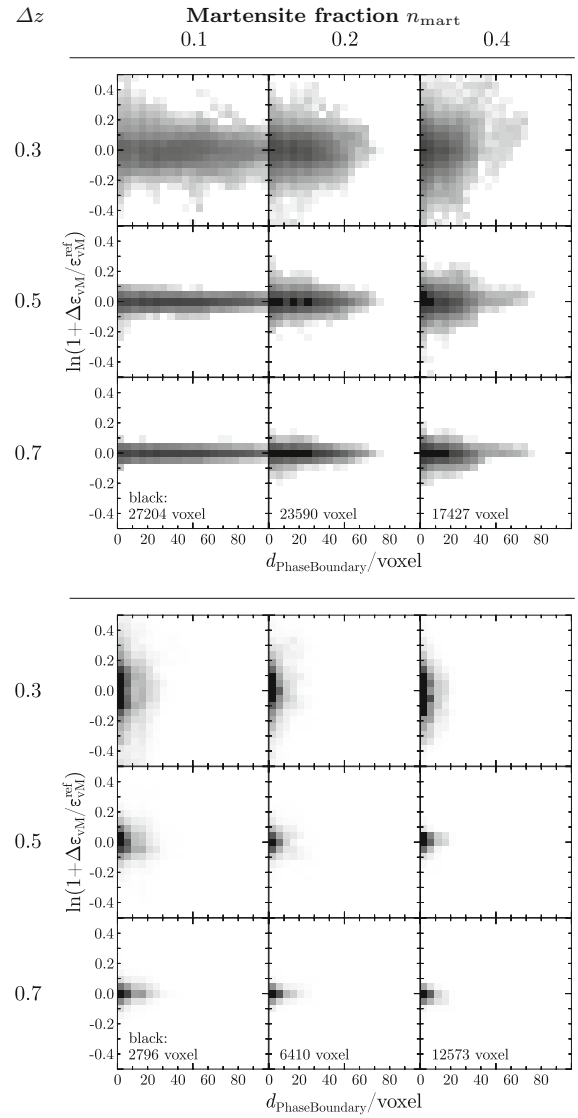


**Fig. 10** Correlation between relative strain change and distance to a phase boundary for ferrite (*top*) and martensite (*bottom*) resulting from grain shape variation at $\Delta z = 0.3, 0.5, 0.7$ with $n_{mart} = 0.1, 0.2, 0.4$

observed as shown for microstructure B at $z = 0.5$ in Fig. 11. This deviation is progressively increasing with increasing columnarity and results in the strongest heterogeneity of strain and stress for $h = 0.01$. The stress pattern appears to be rather random while strain accumulates in deformation bands such that no obvious correlation between high relative changes in strain and stress is observable. The strain localization grows with increasing columnarity as well as increasing martensite content and results in clearly visible distortions (in particular for $n_{mart} = 0.4$ and $h = 0.01$). The amplification of strain partitioning towards the columnar microstructure renders this simplification especially unsuitable for predicting phenomena that strongly depend on local quantities, e.g. damage. An interesting observation can be made in Fig. 12 for the relative strain change of martensite (bottom). The hard phase within a strictly columnar two-phase structure shows a systematic trend of generally increased strains at low volume fraction to generally decreased strains at high volume fraction

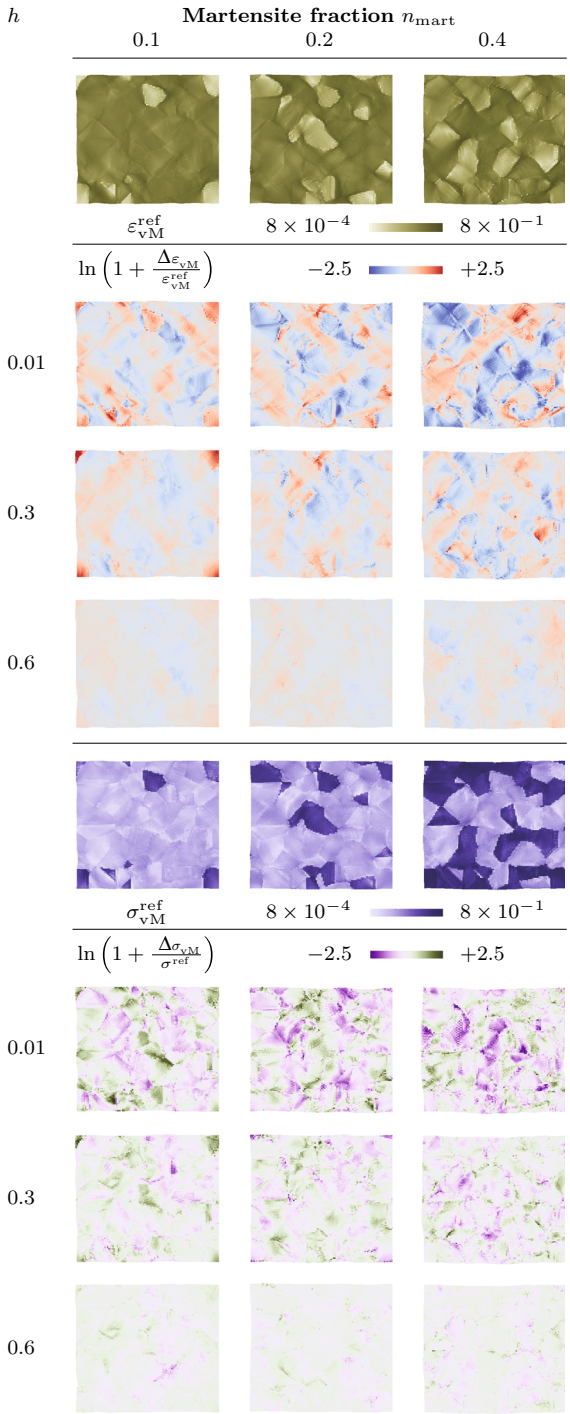


**Fig. 11** $\varepsilon_{\mathrm{vM}}^{\mathrm{ref}}$ (*top*) and $\sigma_{\mathrm{vM}}^{\mathrm{ref}}$ (*bottom*) of microstructure B at $z = 1$ and the sequence of relative strain and stress changes resulting from grain columnarity variation at $h = 0.01$, 0.3, and 0.6 with $n_{\mathrm{mart}} = 0.1$, 0.2, 0.4

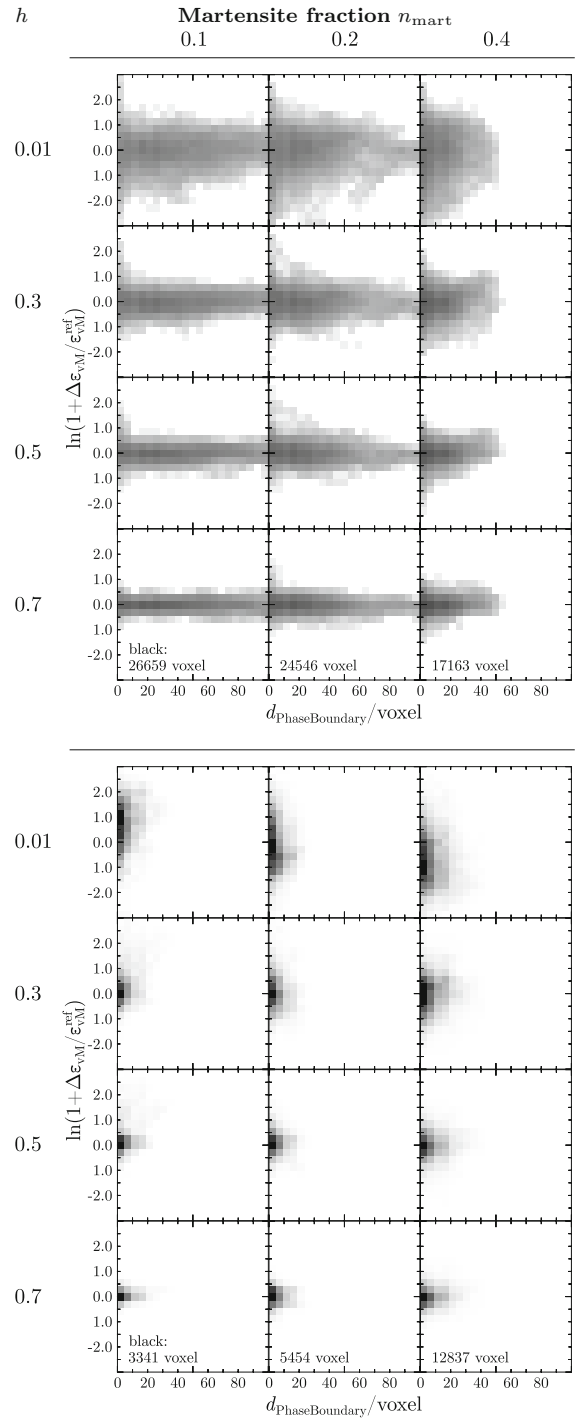


**Fig. 12** Correlation between relative strain change and distance to a phase boundary for ferrite (*top*) and martensite (*bottom*) resulting from grain columnarity variation at $h = 0.01$, 0.3, 0.5, and 0.7 with $n_{\mathrm{mart}} = 0.1$, 0.2, and 0.4

relative to the same volume fractions loaded in a 3D equiaxed configuration ($\Delta\varepsilon_{vM} > 0$ at $n_{mart} = 0.1$ and $\Delta\varepsilon_{vM} < 0$ at $n_{mart} = 0.4$ for $h = 0.01$). A possible explanation could be that isolated martensite grains in a soft ferrite matrix need to strain only very little in a 3D configuration, since their lower deformation accommodation can be compensated in the immediately surrounding ferrite matrix. This capability for compensation by the matrix is substantially curtailed in a columnar structure since phase variability along the third dimension is lost. The opposite response seen for high volume fractions of martensite could be related to the hard phase in a 2D structure having higher effective contiguities than the same volume fraction distributed in a 3D equiaxed structure. As a consequence, the increased probability for the development of load-carrying force chains among martensite grains will result in a stiffer response in columnar cases, i.e. $\Delta\varepsilon_{vM} < 0$.

## 4 Conclusion and outlook

The presented study underlines—in accordance with the findings of Zeghadi et al. [28, 29]—the relevance of subsurface microstructural features on the stress and strain partitioning observed on a surface. For the equiaxed grain structures investigated in this work, structural changes farther than about 3 average grain sizes away from a region of interest (ROI), for instance the surface, can be considered of negligible importance for the stress and strain partitioning in the ROI. This interaction distance is systematically increasing with increasing volume fraction of hard phase (here martensite in a ferritic matrix). Local fields of stress and strain are more sensitive to the phase distribution of neighboring grains than to their crystallographic orientation. This indicates that, especially for complex microstructures, surface observations are hard to interpret at the scale of individual grains when the underlying microstructure (particularly the phase distribution) is not known.

The assumption of a columnar grain structure introduces a strong simplification that results in an amplification of the stress and strain partitioning, particularly in the case of composite materials consisting of hard and soft phases. Therefore, predictions of strongly localized effects, such as damage, based on 2D simulations of heterogeneous microstructures can be highly misleading.

**Acknowledgments** This research was carried out under Project Number M 41.2.10410 in the framework of the Research Program of the Materials innovation institute (M2i) (www.m2i.nl).

## References

1. Brisard S, Dormieux L (2010) FFT-based methods for the mechanics of composites: a general variational framework. Comput Mater Sci 49(3):663–671. doi:10.1016/j.commatsci.2010.06.009
2. Chen P, Ghassemi-Armaki H, Kumar S, Bower A, Bhat S, Sadagopan S (2014) Microscale-calibrated modeling of the deformation response of dual-phase steels. Acta Mater 65:133–149. doi:10.1016/j.actamat.2013.11.036
3. Eisenlohr P, Diehl M, Lebensohn RA, Roters F (2013) A spectral method solution to crystal elasto-viscoplasticity at finite strains. Int J Plast 46:37–53. doi:10.1016/j.ijplas.2012.09.012
4. Eyre DJ, Milton GW (1999) A fast numerical scheme for computing the response of composites using grid refinement. Eur Phys J Appl Phys 6(1):41–47. doi:10.1051/epjap:1999150
5. Hutchinson JW (1976) Bounds and self-consistent estimates for creep of polycrystalline materials. Proc R Soc A 348:101–127. doi:10.1098/rspa.1976.0027
6. Lahellec N, Michel JC, Moulinec H, Suquet P (2001) Analysis of inhomogeneous materials at large strains using fast Fourier transforms. In: Miehe C (ed) IUTAM symposium on computational mechanics of solid materials at large strains, vol 108. Kluwer, Dordrecht, pp 247–258. doi:10.1007/978-94-017-0297-3_22
7. Landron C, Bouaziz O, Maire E, Adrien J (2013) Experimental investigation of void coalescence in a dual phase steel using X-ray tomography. Acta Mater 61(18):6821–6829. doi:10.1016/j.actamat.2013.07.058
8. Lebensohn RA (2001) N-site modeling of a 3D viscoplastic polycrystal using fast Fourier transform. Acta Mater 49(14):2723–2737. doi:10.1016/S1359-6454(01)00172-0
9. Lebensohn RA, Castelnau O, Brenner R, Gilormini P (2005) Study of the antiplane deformation of linear 2-D polycrystals with different microstructures. Int J Solids Struct 42(20):5441–5459. doi:10.1016/j.ijsolstr.2005.02.051
10. Lebensohn RA, Rollett AD, Suquet P (2011) Fast fourier transform-based modeling for the determination of micromechanical fields in polycrystals. JOM 63(3):13–18. doi:10.1007/s11837-011-0037-y
11. Lebensohn RA, Kanjarla AK, Eisenlohr P (2012) An elasto-viscoplastic formulation based on fast Fourier transforms for the prediction of micromechanical fields in polycrystalline materials. Int J Plast 32–33:59–69. doi:10.1016/j.ijplas.2011.12.005
12. Lefebvre G, Sinclair CW, Lebensohn RA, Mithieux JD (2012) Accounting for local interactions in the prediction of roping of ferritic stainless steel sheets. Model Simul Mater

Sci Eng 20(2):024,008. doi:10.1088/0965-0393/20/2/024008
13. Michel JC, Moulinec H, Suquet P (2001) A computational scheme for linear and non-linear composites with arbitrary phase contrast. Int J Numer Methods Eng 52(12):139–160. doi:10.1002/nme.275
14. Monchiet V, Bonnet G (2012) A polarization-based FFT iterative scheme for computing the effective properties of elastic composites with arbitrary contrast. Int J Numer Methods Eng 89(11):1419–1436. doi:10.1002/nme.3295
15. Moulinec H, Suquet P (1994) A fast numerical method for computing the linear and nonlinear properties of composites. Comptes rendus de l'Académie des Sciences Série II, Mécanique, Physique, Chimie, Astronomie 318:1417–1423
16. Oosterlee CW, Washio T (2000) Krylov subspace acceleration of nonlinear multigrid with application to recirculating flows. SIAM J Sci Comput 21(5):1670–1690. doi:10.1137/S1064827598338093
17. Ramazani A, Mukherjee K, Quade H, Prahl U, Bleck W (2013) Correlation between 2D and 3D flow curve modelling of DP steels using a microstructure-based RVE approach. Mater Sci Eng A 560:129–139. doi:10.1016/j.msea.2012.09.046
18. Ramazani A, Ebrahimi Z, Prahl U (2014) Study the effect of martensite banding on the failure initiation in dual-phase steel. Comput Mater Sci 87:241–247. doi:10.1016/j.commatsci.2014.01.051
19. Roters F, Eisenlohr P, Hantcherli L, Tjahjanto DD, Bieler TR, Raabe D (2010) Overview of constitutive laws, kinematics, homogenization, and multiscale methods in crystal plasticity finite element modeling: theory, experiments, applications. Acta Mater 58:1152–1211. doi:10.1016/j.actamat.2009.10.058
20. Shanthraj P, Eisenlohr P, Diehl M, Roters F (2015) Numerically robust spectral methods for crystal plasticity simulations of heterogeneous materials. Int J Plast 66:31–45. doi:10.1016/j.ijplas.2014.02.006
21. Suquet P, Moulinec H, Castelnau O, Montagnat M, Lahellec N, Grennerat F, Duval P, Brenner R (2012) Multi-scale modeling of the mechanical behavior of polycrystalline ice under transient creep. In: Procedia IUTAM: IUTAM symposium on linking scales in computation: from microstructure to macroscale properties 3, pp 64–78. doi:10.1016/j.piutam.2012.03.006
22. Tasan CC, Diehl M, Yan D, Zambaldi C, Shanthraj P, Roters F, Raabe D (2014) Integrated experimental-numerical analysis of stress and strain partitioning in multi-phase alloys. Acta Mater 81:386–400. doi:10.1016/j.actamat.2014.07.071
23. Tasan CC, Hoefnagels JPM, Diehl M, Yan D, Roters F, Raabe D (2014) Strain localization and damage in dual phase steels investigated by coupled in-situ deformation experiments-crystal plasticity simulations. Int J Plast 63:198–210. doi:10.1016/j.ijplas.2014.06.004
24. Tasan CC, Diehl M, Yan D, Bechtold M, Roters F, Schemmann L, Zheng C, Peranio N, Ponge D, Koyama M, Tsuzaki K, Raabe D (2015) An overview of dual-phase steels: advances in microstructure-oriented processing and micromechanically guided design. Ann Rev Mater Res 45:391–431. doi:10.1146/annurev-matsci-070214-021103
25. Tjahjanto DD, Turteltaub S, Suiker ASJ (2008) Crystallographically based model for transformation-induced plasticity in multiphase carbon steels. Contin Mech Thermodyn 19(7):399–422. doi:10.1007/s00161-007-0061-x
26. Zambaldi C, Raabe D (2010) Plastic anisotropy of $\gamma$-TiAl revealed by axisymmetric indentation. Acta Mater 58(9):3516–3530. doi:10.1016/j.actamat.2010.02.025
27. Zambaldi C, Yang Y, Bieler TR, Raabe D (2012) Orientation informed nanoindentation of $\alpha$-titanium: indentation pileup in hexagonal metals deforming by prismatic slip. J Mater Res 27(1):356–367. doi:10.1557/jmr.2011.334
28. Zeghadi A, Forest S, Gourgues AF, Bouaziz O (2007a) Ensemble averaging stress–strain fields in polycrystalline aggregates with a constrained surface microstructure—Part 2: crystal plasticity. Philos Mag 87(8–9):1425–1446. doi:10.1080/14786430601009517
29. Zeghadi A, N'guyen F, Forest S, Gourgues AF, Bouaziz O (2007b) Ensemble averaging stress–strain fields in polycrystalline aggregates with a constrained surface microstructure—Part 1: anisotropic elastic behaviour. Philos Mag 87(8–9):1401–1424. doi:10.1080/14786430601009509
30. Zeman J, Vondřejc J, Novák J, Marek I (2010) Accelerating a FFT-based solver for numerical homogenization of periodic media by conjugate gradients. J Comput Phys 229(21):8065–8071. doi:10.1016/j.jcp.2010.07.010